Chinese Chemical Letters 35 (2024) 110020

Contents lists available at ScienceDirect

Chinese Chemical Letters

journal homepage: www.elsevier.com/locate/cclet

Imaging polarity changes in pneumonia and lung cancer using a lipid droplet-targeted near-infrared fluorescent probe

Huamei Zhang[a,1], Jingjing Liu[b,1], Mingyue Li[a], Shida Ma[a], Xucong Zhou[a], Aixia Meng[a], Weina Han[a,*], Jin Zhou[a,*]

[a] School of Pharmacy, School of Basic Medical Sciences, Shandong Second Medical University, Weifang 261053, China
[b] Department of Respiratory and Critical Care Medicine, Weifang People's Hospital (The First Affiliated Hospital of Shandong Second Medical University), Weifang 261041, China

ARTICLE INFO

Article history:
Received 7 April 2024
Revised 6 May 2024
Accepted 15 May 2024
Available online 16 May 2024

Keywords:
Fluorescent probe
Lipid droplets
Polarity
Pneumonia
Lung cancer

ABSTRACT

As the main organ of gas exchange, the lungs are susceptible to various exogenous attacks, and pneumonia is one of the major inflammatory diseases that threaten human health. Generally, pneumonia is a disease that occurs in the alveoli and respiratory bronchioles induced by pathogens and further causes local and systemic inflammatory responses. The development of pneumonia can bring various serious complications, including lung abscess, sepsis, meningitis, brain damage and hearing loss. Over the past few decades, the mortality rate of pneumonia patients has remained high. While lung cancer is another lung-related malignant tumors worldwide, with a low 5 year survival rate. Exploring the mechanisms of their occurrence and interaction between pneumonia and lung cancer is a challenging and meaningful task. The abnormalities of lipid droplets (LDs) polarity have been found strongly accompanied by many diseases, especially cancer, inflammation, and metabolic diseases. However, their exact role is not yet clear. Hence, it is significant to develop a novel detection method to observe the polarity changes of LDs, which would help to reveal the development process of diseases pneumonia and lung cancer. In this work, a new polarity-sensitive LDs-targeted near-infrared probe **BFZ** up to 712 nm was designed, according to the intramolecular charge transfer mechanism, which displayed high fluorescence intensity in low polarity while showing decreased fluorescence intensity in high-polarity conditions with a significant redshift. The **BFZ** was successfully applied to the change of LDs polarity in lipopolysaccharide (LPS)-stimulated A549 cells, and a mouse model of lung inflammation. It also tells the polarity differences between normal and tumor cells and between normal and tumor tissues. Moreover, the correlations between pneumonia and polarity changes were observed through the imaging experiments, which may provide an insightful method for the early diagnosis of pneumonia and lung cancer.

Inflammation is the body's integral and natural response to signals caused by tissue damage or pathogen invasion [1,2]. As a two-side sword, inflammation serves as an adaptive response to maintain homeostasis when the organism is traumatized or infected by blocking pathogens or repairing damaged tissue; on the other hand, when there is an imbalance in the body's homeostasis, inflammation can develop into an uncontrollable or chronic process that eventually leads to a variety of inflammatory diseases. Depending on the site of the infected organ, the type of inflammatory diseases can be categorized as pneumonia, arthritis, encephalitis, rhinitis, gastroenteritis, *etc.* [2]. As the main organ of gas exchange, the lungs are susceptible to various exogenous attacks, and pneumonia is one of the major inflammatory diseases that threaten human health. In general, pneumonia is a disease of the alveoli and bronchi caused by pathogens that enter the body through the respiratory route. The invasion of pathogens causes the body to exhibit local and systemic inflammatory reactions [3-5]. Pneumonia may be associated with multiple serious complications, including lung abscess, sepsis, meningitis, and brain injury [6]. Over the past few decades, mortality in patients with pneumonia has been increasing over the long-term course of the disease. Therefore, early detection and timely treatment of pneumonia is very important. Current traditional computed tomography (CT) and chest X-ray imaging methods for the clinical diagnosis of pneumonia are not only expensive, but they can also jeopardize human

* Corresponding authors.
E-mail addresses: starhwn@sdsmu.edu.cn (W. Han), zhoujin@sdsmu.edu.cn (J. Zhou).
[1] These authors contributed equally to this work.

https://doi.org/10.1016/j.cclet.2024.110020
1001-8417/

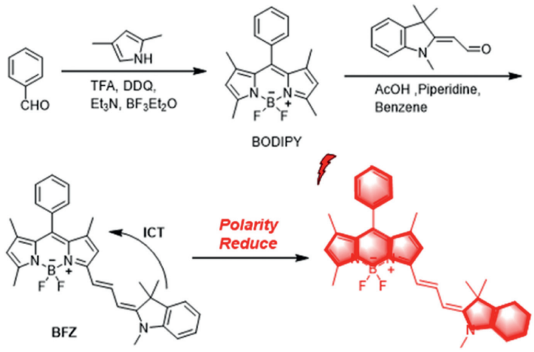

Scheme 1. Synthesis and fluorescence response of **BFZ** to polarity.

health such as causing cancer, germ cell abnormalities and chromosomal disorders [5]. Therefore, the development of a safe visual imaging method for early detection of pneumonia disease is essential.

Inflammation, a complex pathological process that also underlies the development of various diseases, is accompanied by alterations in the cellular microenvironment, of which polarity is one of the critical parameters [7,8]. Cell polarity reflects a series of complex mechanisms and is one of the important parameters for establishing specific functional domains and maintaining normal cellular functioning. Diseases caused by cellular processes, such as permeability of membrane compartments, directional migration, and activation of immune responses, affect the changes and development of diseases and are often interconnected with polarity [9,10]. Polarity changes in different regions have been recognized as reliable indicators of different diseases [11,12]. It has been demonstrated that when inflammation occurs in the organism, there is a corresponding change in local polarity [13,14]. Lipid droplets (LDs) are specialized organelles that store lipids and are encapsulated by a neutral lipid core and a monolayer of phospholipids, as well as a number of specialized surface proteins such as periplasmic lipoproteins. LDs are considered to be dynamic organelles, which are related to lipid storage and metabolism, signaling, apoptosis, *etc.* In addition to that, linkages between LDs and other organelles were also observed [15,16]. For instance, lipophagy is a process of degradation of LDs by lysosomes in which abnormal LDs are catabolized in lysosomes to maintain homeostasis in the cellular environment. The abnormal changes in the polarity of LDs have been shown to be associated with a variety of diseases, such as cancer, inflammatory diseases, and metabolic diseases [17,18]. Lipid metabolism undergoes reprogramming in cancer cells compared to healthy cells, resulting in the prominent feature of accumulation of LDs in carcinoma cells [19]. Lung cancer is one of the malignant tumors with the highest incidence rate and mortality rate in the world, and about 80% of lung cancer patients are non-small cell lung cancer (NSCLC), whose 5-year survival rate is only 4%–17% and the definite diagnosis time is in the undesirable middle and late stages for 75% of patients [20]. Therefore, early detection and timely diagnosis of lung cancer are a vital step in improving the survival rate of cancer patients. Fluorescence imaging has become one of the indispensable tools for exploring the process of life activities, both at the cellular level and in the organism to realize *in situ* and real-time detection, for its advantages of non-invasive, high sensitivity and high temporal and spatial resolution [21-27]. Therefore, it is meaningful to design a probe that is sensitive to polarity and targets LDs for monitoring pneumonia and lung cancer during disease progression.

Hereof, a polarity-sensitive near-infrared fluorescent probe (**BFZ**) with good LDs targeting was developed. As shown in Scheme 1, **BFZ** with a D-π-A molecular configuration was synthesized based on a condensation reaction between typical fluoroborodipyrrole parent nucleus and a Fischer aldehyde (1,3,3-trimethyl-2-(formylmethylene)indoline), which exhibits intramolecular charge transfer (ICT) properties. In a low-polarity solution, **BFZ** emits strong fluorescence, and the emission intensity decreases and emission wavelength redshifts significantly with the increase of solution polarity, in a strong polarity-dependent manner. With **BFZ** in hand, we have succeeded in assaying LDs polarity changes stimulated by oleic acid, statins, and lipopolysaccharide (LPS). In addition, the visualization of LDs polarity was explored in the mouse model of pneumonia and lung cancer, which would offer a new research method for the early diagnosis and treatment of pneumonia and lung cancer.

The probe **BFZ** was synthesized with fluoroborondipyrrole (BODIPY) as the electron acceptor (A) and Fischer aldehyde as the donor (D), and the donor and acceptor were connected by a π-bridge. Based on the intramolecular charge transfer mechanism, the probe is anticipated to demonstrate polarity sensitivity. The structure of **BFZ** was characterized by ^{1}H nuclear magnetic resonance spectra (NMR), ^{13}C NMR spectroscopy and high-resolution mass spectrometry, and detailed information is shown in Supporting information.

In view of verifying the response of the probe to the polarity, the photophysical properties of **BFZ** were investigated in solvents with different polar, including dimethyl sulfoxide, dichloromethane, toluene, acetone and 1,4-dioxane. As shown in Fig. 1A and Fig. S4A (Supporting information), in the above solutions, **BFZ** exhibited a clear polarity dependence, and the fluorescence intensity of **BFZ** gradually decreased with increasing solvent polarity accompanied by a redshift; as far as the absorption was concerned (Fig. S4B in Supporting information), the absorption spectra of the probes showed slender variations in different polar media, with absorption peaks mainly around ~650 nm. Thereafter, the correlation between the polarity parameter and the maximum emission wavelength was evaluated [16]. As illustrated in Fig. 1B, there is a good linear correlation between the maximum emission wavelength of the probe and the polarity of the solvent ($R^2 = 0.988$). This further reveals the dependence of emission wavelength and fluorescence intensity on polarity. In comparison with other solvents, it is 1,4-dioxane that would be the best mimic of the biofilm structure [28,29]. The polarity of the test solution system was changed by altering the volume ratio of 1,4-dioxane to water to further demonstrate the polarity sensitivity of the **BFZ** probe. The experimental results illustrated that with the increase of water content in the test system, the fluorescence intensity and emission wavelength of the probe **BFZ** were changed, which was manifested as a gradual weakening of the fluorescence intensity and a red shift of the emission wavelength. In addition, we found that the fluorescence intensity in 0% water is thousands of times higher than that in 90% water. The above results show that the **BFZ** responds well to changes in polarity (Figs. 1C and D). The above results show that **BFZ** responds favorably to changes in polarity. To further show how **BFZ** structural features correlate with polarity, we performed density-functional theory (DFT) calculation at the B3LYP/6–311 G(d, p) level (Fig. 1E). The highest occupied molecular orbital (HOMO) (−4.6872 eV) electrons are essentially concentrated in the Fischer aldehyde module, and the lowest unoccupied molecular orbital (LUMO) (−2.4221 eV) electrons are mainly concentrated in the BODIPY module, with an energy difference of $E_{gap} = 2.2651$ eV between the two. The results of DFT calculations show that the D-π-A structure of **BFZ** enables intramolecular charge transfer. The probe exhibits weak fluorescence in highly polar environments since the excited state energy could be dissipated *via* non-radiative relaxation pathways, whereas strong fluorescence emission occurs in non-polar media. Some details about DFT calculation are provided in Table S1 (Supporting information).

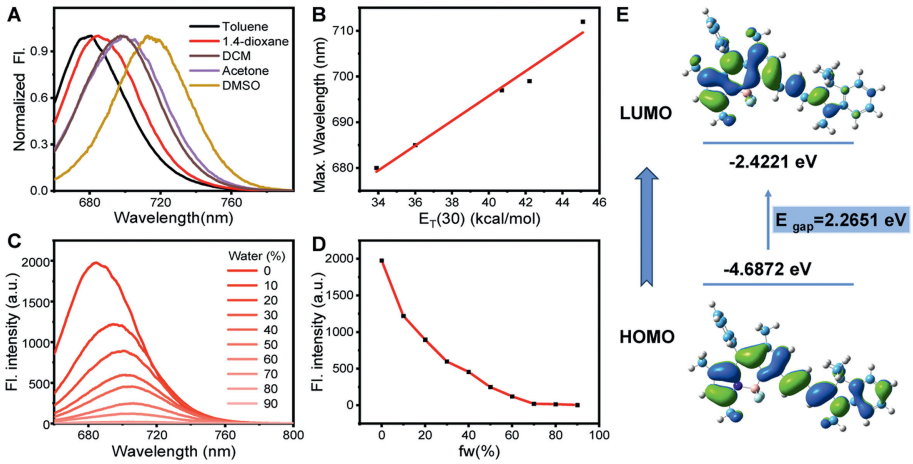

Fig. 1. (A) Normalized spectra of **BFZ** (10 μmol/L) in different polar solvents. (B) Plot of the emission wavelength maximum of **BFZ** in various solvents *vs.* $E_T(30)$. (C) Emission fluorescence spectra of **BFZ** in different polarities of a 1,4-dioxane/H_2O system with the fraction of H_2O (fw) ranging from 0 to 90%. (D) Fluorescence intensity at of **BFZ** as a function of fw. $\lambda_{ex} = 645$ nm. (E) LUMO and HOMO of **BFZ** by DFT calculations at the base level of B3LYP/6–311 G (d, p) *via* the Gaussian 16 program.

To test the polarity specificity of the **BFZ**, we investigated whether the **BFZ** has the basic ability to counteract interference from relevant bioactive molecules, such as metal ions (Fe^{3+}, Mg^{2+}, Ca^{2+}, and Zn^{2+}, *etc.*), reactive oxygen species (ROS) ($ONOO^-$, ClO^-, and $O_2^{\bullet-}$, *etc.*), amino acids (Hcy, GSH, and Cys, *etc.*), and enzyme (alkaline phosphatase). As shown in Fig. S5 (Supporting information), the fluorescence intensity of **BFZ** remains essentially constant when all types of interfering materials are present. On the contrary, a stronger fluorescence intensity was exhibited in 1,4-dioxane. Thus, in complex biological systems, the **BFZ** does not respond to biologically active substances and has a high environmental polarity-specific capacity.

Given that polarity-sensitive molecules usually also exhibit some sensitivity to viscosity, which may affect the determination of polarity based on the maximum emission value, we investigated the fluorescence response of **BFZ** in mixed solvents with different ratios of water and glycerol. It was found that the fluorescence intensity rose only slightly with increasing viscosity (Fig. S6 in Supporting information), which in turn ruled out the potential interference of viscosity. Determination of a suitable pH range is essential for the application of the probe. The photophysical behavior of **BFZ** in the pH range of 3.41–11.43 pH was investigated. As shown in Fig. S7 (Supporting information), in the range of pH 3.41–11.43, **BFZ** shows a minimal change in fluorescence intensity, indicating that the probe would not be affected by pH. Photostability is one of the important features that need to be tested when imaging probes at the cellular level. Therefore, we investigated the photostability tests of **BFZ** in three mixed solutions with different polarities (1,4-dioxane, 40% 1,4-dioxane, 80% 1,4-dioxane), the fluorescence intensity of **BFZ** was essentially stable in all three solutions, suggesting that the probe **BFZ** is remarkably photostable (Fig. S8 in Supporting information), when its fluorescence intensity remained stable from 22 °C to 40 °C (Fig. S9 in Supporting information). It indicates that the probe has good stability and it has great potential for real-time dynamic imaging. Triglycerides are the main component of LDs. Thus, glyceryl trioleate including medium-chain triglycerides was used as a model substance for LDs [30]. As displayed in Fig. S10 (Supporting information), **BFZ** produces a considerable quantity of red fluorescence in glyceryl trioleate with excellent fluorescence intensity; however, after adding a certain amount of glycerol trioleate to the solution to form an oil/water (O/W) emulsion [30], fluorescence response still depends on glyceryl trioleate concentration. As the concentration of glycerol trioleate increased from 0 to 700 μg/mL, **BFZ** fluorescence steadily increased. Therefore, **BFZ** can be used to detect LDs.

Before applying **BFZ** to bioimaging, we evaluated its effects on five types of cells, including A549 cells (human non-small cell lung cancer cells), MCF-7 cells (human breast cancer cells), HepG2 cells (human hepatocellular carcinoma cells), HTR-8 cells (human chorionic trophoblast cells), and L02 cells (normal human liver cells) by MTT assay. When the concentration of the probe was 25 μmol/L, the toxicity of **BFZ** on the above cells remained over 80%, indicating that the cytotoxicity of **BFZ** was low (Fig. S11 in Supporting information). Next, time-dependent imaging and photostability imaging of **BFZ** were investigated at the cellular level. As shown in Fig. S12 (Supporting information), the probe was co-incubated with A549 cells and imaged at 10 min intervals, which showed that the probe could enter the cells efficiently and reached equilibrium around 30 min. In addition, under continuous laser irradiation, we found that the fluorescence signal of **BFZ** inside the cells stayed virtually untouched after 16 min of irradiation (Fig. S13 in Supporting information). To test whether the **BFZ** probe could distinguish normal from cancerous cells based on differing intracellular polarity, four different cell lines including MCF-7 cells, HeLa cells (human cervical cancer cells), L02 cells and HTR-8 cells were selected for fluorescence confocal imaging experiments, and as shown in Figs. S14A and B (Supporting information), the fluorescence signals of cancer cells (HeLa and MCF-7 cells) were higher than that of normal cells in red fluorescence channels cells (L02 cells and HTR-8 cells). Experiments using flow cytometry on the same treated cells yielded consistent results (Fig. S14C in Supporting information). The results indicate that the probe **BFZ** can be used to recognize normal cells and cancer cells based on the differences in intracellular polarity.

Next, the subcellular localization of the probe **BFZ** in living cells was investigated, and **BFZ** were co-incubated with the commercial dyes ERTG (a pro-endoplasmic reticulum dye), BODIPY493/503 (a commercially available LD targeting dye), Hoechst 33,342 (a commercial nuclear staining dye), LTG (a commercial lysosome staining dye), MTG (a commercial mitochondria-staining dye) in A549 cells. As seen in Figs. S15A–E (Supporting information), **BFZ** exhibited clear spherical spot morphologies and overlapped well with BODIPY 493/503 with the Pearson coefficients in the cell above 0.80, which suggests that the probe has significant LDs-targeting ability. Conversely, **BFZ** costained with ERTG, Hoechst 33,342, Lyso Tracker Green DND-26 and Rhodamine 123 in A549 cells showed weak colocalization imaging with a low PC of 0.52, 0.14, 0.40 and

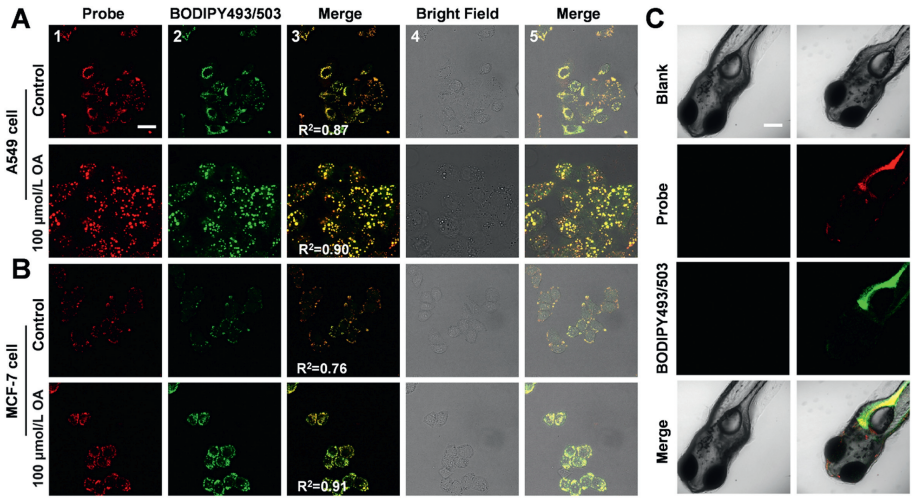

Fig. 2. Co-localization imaging of **BFZ** and BODIPY 493/503 for imaging two cell lines (A549 cells and MCF-7 cells) pretreated with OA. (A) A549 cells pretreated with OA (100 μmol/L) co-localization imaging of **BFZ** (1 μmol/L) and BODIPY 493/503 (2 μmol/L). (B) MCF-7 cells pre-treated with OA (100 μmol/L) co-localization imaging of **BFZ** (1 μmol/L) and BODIPY 493/503 (2 μmol/L). (1) The red channel of **BFZ**, (2) the green channel of BODIPY, (3) the merge of 1 and 2, (4) the bright field channel, (5) the merge of 3 and 4. (C) Co-localization imaging of untreated zebrafish (left) as the control, and zebrafish stained with **BFZ** and BODIPY 493/503 (right). Red channel: $\lambda_{ex} = 633$ nm, $\lambda_{em} = 650–750$ nm for **BFZ**; Green channel; $\lambda_{ex} = 496$ nm, $\lambda_{em} = 500–600$ nm for BODIPY 493/503. Scale bar: 30 μm.

0.44 (Figs. S15F–J in Supporting information), respectively, and the intensity distributions of the corresponding ROIs representing **BFZ** and market dyes were significantly shifted (Fig. S15). We then performed the co-localization imaging experiments with oleic acid (OA) stimulation to further validate the LDs targeting performance of the probe **BFZ**. OA in cells can be converted to triglycerides to stimulate the cell to produce large amounts of LDs, hence serving as LDs inducer [32]. In co-localization experiments, 100 μmol/L OA was added to the cell culture medium to stimulate the cells before imaging, and then **BFZ** and BODIPY 493/503 were co-incubated with A549 cells for confocal imaging, which showed that after stimulation with OA, LDs were detected in the green channel corresponding to BODIPY 493/503 and in the red channel corresponding to **BFZ**, compared to the control group. The number of lipid droplets and fluorescence intensity increased, at which time the co-localization coefficient was 0.90 (Fig. 2A). The same result was observed in MCF-7 cells (Fig. 2B). The above experiments show that **BFZ** has a good ability to target lipid droplets.

Zebrafish and humans have similar genetic characteristics and are often used to study *in vivo* imaging [31]. We investigated *in vivo* imaging of LDs in zebrafish using the probe **BFZ**. As displayed in Fig. 2C, the control zebrafish, which has no treatment, exhibited almost no fluorescence in both channels (496 and 633 nm) under the laser confocal microscope. In comparison, when the zebrafish were co-incubated with BODIPY 493/503 and **BFZ** at room temperature, bright green (BODIPY 493/503 fluorescence emission) and red (**BFZ** fluorescence emission) signals could be observed in the corresponding channel respectively. Furthermore, the high coincidence degree between the two channels further confirmed our probe **BFZ** has a great potential for tracing LDs in zebrafish. In addition, we also found that the fluorescence intensity of A549, CNE (human nasopharyngeal carcinoma cell), MCF-7 and PANC02-H7 (mouse pancreatic cancer cell) cells increased significantly after co-incubation with oleic acid, respectively, suggesting that it is the intracellular polarity that is decreased (Figs. 3A–D). Experiments using flow cytometry on the same treated cells yielded consistent results (the rightmost column of Figs. 3A–D). The above results indicate that the probe **BFZ** can efficiently stain LDs in cells, and that it is possible to monitor the variation in the values of LDs in different states as well as the decrease in intracellular polarity due to the increase in the number of intracellular LDs.

LDs are multioctave organelles that are intimately associated with organelles including lysosomes. The process of LDs-lysosome interaction is known as lipophagy, in which the lysosome maintains cellular homeostasis by phagocytosing dysfunctional LDs [32]. Then **BFZ** was used to track the dynamic LD behaviors during lipophagy induced by starvation in living A549 cells. Cells were pre-treated with 1 μmol/L **BFZ** and 2 μmol/L Lyso Tracker Green and kept in starvation for confocal imaging during the time series. Under continuous starvation conditions, the colocalization coefficient increased from 0.44 to 0.51, and this phenomenon suggested that contact between lipid droplets and lysosomes increased during prolonged starvation. Damaged LDs were probably phagocytosed by lysosomes (Fig. S16 in Supporting information). LDs are the main storage site for cellular neutral lipids, which consist mainly of triacylglycerols, diacylglycerols, cholesterol and their esters [33]. Statins are a class of cholesterol-lowering drugs known as 3–hydroxy-3-methyl-glutaryl coenzyme A (HMG-CoA) reductase inhibitors. Not only do they lower blood cholesterol levels and reduce the risk of cardiovascular disease, but they may also play an important role in the prevention and treatment of lung cancer [34]. Therefore, we investigated the effect of three different statins (rosuvastatin, simvastatin and atorvastatin) on intracellular LDs in A549 cells. A549 cells were incubated with simvastatin (20 and 40 μmol/L) for 20 h and then imaged by probe incubation for 30 min. In comparison with the group control, the number of intracellular LDs in simvastatin-treated cells with different concentrations of simvastatin was significantly reduced and the fluorescence intensity was weakened (Fig. 3E), while rosuvastatin and atorvastatin also showed different degrees of fluorescence intensity reduction (Figs. 3F and G). Furthermore, the tendency of the fluorescence to change was also clearly reflected in the fluorescence intensity maps (Figs. S17–S19 in Supporting information). The results indicated that the number of intracellular LDs declined or intracellular polarity was enhanced after treatment with the three drugs. We hypothesized that it might be due to the different chemical structures, pharmacokinetic characteristics and potency of simvastatin, atorvastatin and rosuvastatin, which in turn exhibited different effects on LDs. LPS is commonly used to induce acute inflammation and cause changes in the polarity of cellular LDs [35]. A549 cells were incubated with different concentrations of LPS (0, 6, 18 μg/mL) for 12 h, and then treated with 1 μmol/L **BFZ** for 30 min

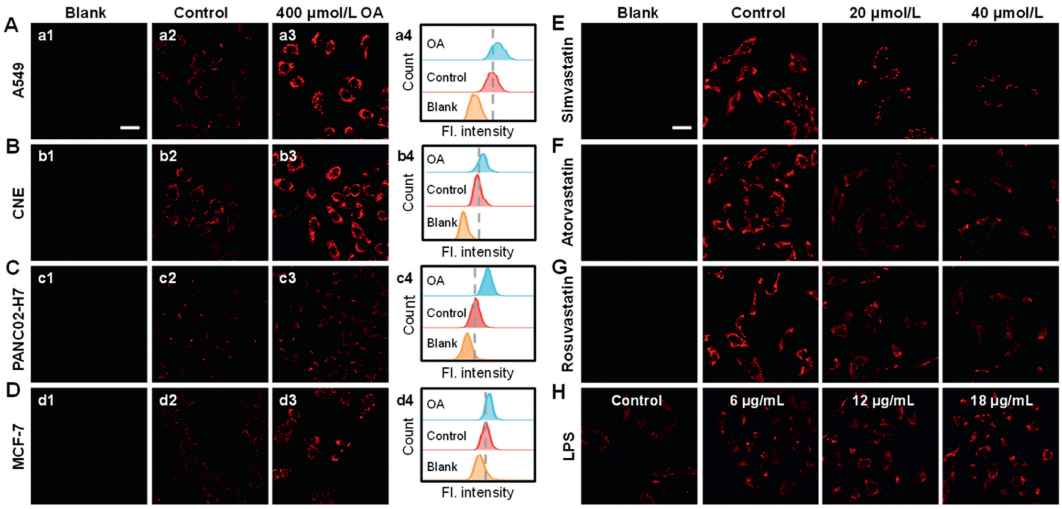

Fig. 3. Fluorescence imaging of cells under different drug stimulation. (A–D) Confocal imaging of different cells (A549, CNE, PANC02-H7, MCF-7 cell). a1–d1: normally cultured A549, CNE, PANC02-H7, MCF-7 cells without probe; a2–d2: different cells incubated with **BFZ** (1 μmol/L) for 30 min; a3–d3: 400 μmol/L oleic acid pretreatment for 2 h followed by 30 min incubation with **BFZ**; a4–d4: Flow cytometric analysis of the above cells. Fluorescence imaging of LDs in A549 cells by simvastatin (E), atorvastatin (F) and rosuvastatin (G). First column: blank group. Second column: control group, cells treated with **BFZ** (1 μmol/L). Third column: cells were pretreated with 20 μmol/L of different drugs (simvastatin, atorvastatin, rosuvastatin) for 20 h and then stained with **BFZ** (1 μmol/L). Fourth column: Cells were pretreated with 40 μmol/L different drugs (simvastatin, atorvastatin, rosuvastatin) for 20 h and then stained with **BFZ** (1 μmol/L). (H) Fluorescence images of **BFZ** (1 μmol/L) in A549 cells as a function of LPS concentration (from left to right LPS concentrations were 0, 6, 12, and 18 μg/mL). Red channel: $\lambda_{ex} = 633$ nm, $\lambda_{em} = 649–751$ nm. Scale bar: 30 μm.

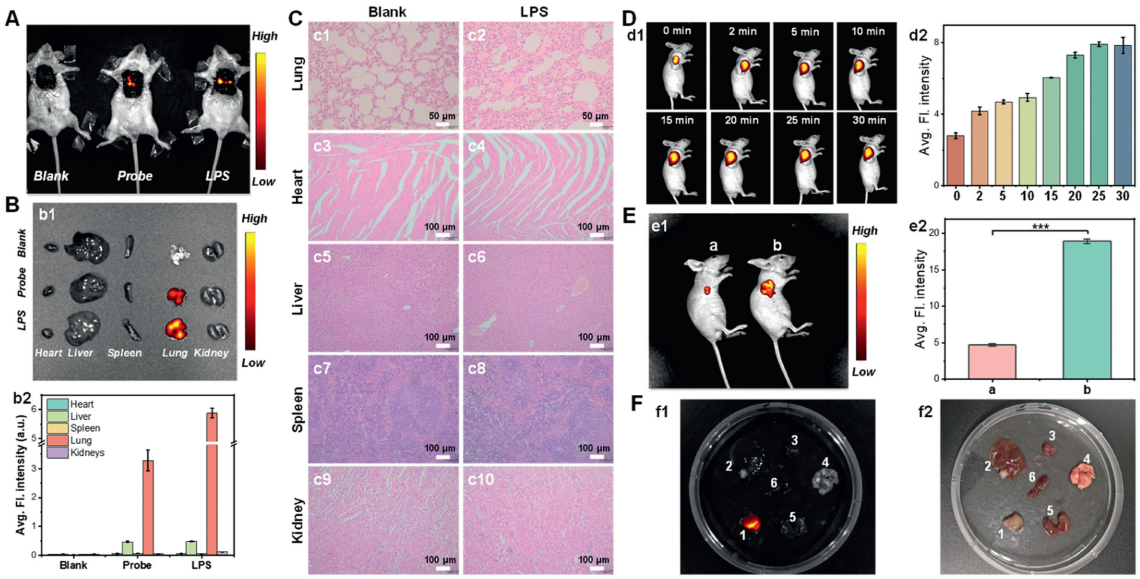

Fig. 4. (A) Fluorescence imaging of a mouse model of pneumonia. (B) (b1) *Ex vivo* fluorescence images of representative organs (from left to right, heart, liver, spleen, lung and kidney). (b2) Relative pixel intensity of b1. (C) H&E results of frozen sections of heart, liver, spleen, lung, and kidney tissues from normal and pneumonia mice. (D) (d1) Time-dependent fluorescence intensities of A549-tumor-bearing BALB/c-nude mice after injection of **BFZ**. (d2) Fluorescence images for the data in (d1). (E) Images of (a) normal BALB/c-nude mice after injection of **BFZ** and (b) A549-tumor-bearing BALB/c-nude mice. (e2) Relative fluorescence intensities of mice a and b. (F) (f1) fluorescence imaging and (f2) *ex vivo* photographs of isolated organs (1. tumor, 2. liver, 3. heart, 4. lung, 5. kidney, 6. spleen). Data are presented as mean ± standard deviation (SD) ($n = 3$). $^{***}P < 0.001$.

as shown in Fig. 3H and Fig. S20 (Supporting information), the fluorescence intensity of the LPS concentration was increased and the changes in fluorescence intensity confirmed the relationship between polarity and acute inflammation.

We subsequently investigated the ability of **BFZ** to detect polarity in a mouse model of pneumonia. All the *in vivo* experimental procedures were approved by the Animal Ethical Experimentation Committee of Shandong Second Medical University and were performed strictly in accordance with the guidance of the National Act on the use of experimental animals. As shown in Fig. 4A and Fig. S21 (Supporting information), the fluorescence signals of lung tissues from LPS-treated mice were significantly stronger than those from normal and blank mice under the same imaging conditions. The *ex vivo* fluorescence imaging was further examined by removing major organs from the control group, probe group, and LPS group, the *ex vivo* results showed that the fluorescence intensity of lung tissues from inflamed mice was significantly higher than that of control and blank mice (Fig. 4B). The output graph more visually shows the difference in fluorescence. Hematoxylin-eosin staining (H&E) of the major organs of mice showed blurred morphology, alveolar congestion, thickening or disappearance of alveolar septa, erythrocyte exudation, and inflammatory cell infiltration in LPS-induced mouse lung tissues (Fig. 4C). Next, the ability of the probe **BFZ** to distinguish tumor tissue from normal tissue in mice

was investigated [36-38]. For this purpose, **BFZ** was injected into the A549 tumor region in the axilla of the right forelimb of normal nude mice, and fluorescence changes were observed. We started by monitoring the changes in the fluorescence of A549 tumor-bearing mice at different times after the injection of **BFZ**. As shown in Fig. 4D, the fluorescence signals in the tumors increased significantly with time and stabilized within 30 min. The ability of **BFZ** to differentiate tumors from normal tissue *in vivo* was also investigated, as shown in Fig. 4E, enhanced fluorescence signals were seen in the region of the tumor loaded mice, while the corresponding region of the normal mice showed weaker fluorescence. These results indicate that the probe can effectively distinguish between tumor and normal tissues *in vivo* and that the tumor tissues possess lower polarity, compared to normal tissues. Fluorescence imaging of isolated hearts, livers, spleens, lungs, kidneys, and tumors showed that we observed fluorescent signals within the tumors as shown in Fig. 4F. Therefore, **BFZ** is a promising tool for tumor polarity detection.

In conclusion, a polarity-sensitive, LDs-targeting near-infrared fluorescent probe was designed based on an intramolecular charge transfer mechanism using fluoroborodipyrrole as a fluorophore, and the probe exhibited good photostability, large Stokes shift, biocompatibility, and was not interfered by pH and viscosity, and we also demonstrated that the **BFZ** had a good capacity for LDs targeting in cells and zebrafish and observed changes in the number of droplets. *Via* imaging LDs polarity, both *in vitro* (cells) and *in vivo* (mice), **BFZ** was successfully used to visualize LDs polarity in pneumonia and lung cancer, which provides a method for real-time visualization and monitoring of pneumonia and has potential applications in exploring the role of polarity in polarity-related diseases and physiological processes.

Declaration of competing interest

The authors declare that they have no known competing financial interests or personal relationships that could have appeared to influence the work reported in this paper.

CRediT authorship contribution statement

Huamei Zhang: Investigation. **Jingjing Liu:** Investigation. **Mingyue Li:** Methodology. **Shida Ma:** Software. **Xucong Zhou:** Software. **Aixia Meng:** Resources. **Weina Han:** Validation. **Jin Zhou:** Writing – review & editing, Supervision.

Acknowledgments

We gratefully acknowledge financial support from the National Natural Science Foundation of China (No. 21705120), Natural Science Foundation of Shandong Province, China (Nos. ZR2017LB016, ZR2023MB001), Special Fund for Taishan Scholar Project (No. tsqn202211231), Foundation of Yuandu Scholar and Science and Technology Development Plan Project of Weifang (No. 2022YX095).

Supplementary materials

Supplementary material associated with this article can be found, in the online version, at doi:10.1016/j.cclet.2024.110020.

References

[1] Z. Tu, Y. Zhong, H. Hu, et al., Nat. Rev. Mater. 7 (2022) 557–574.
[2] X. Zhang, W.Shu F.Tang, et al., Analyst 148 (2023) 5303–5321.
[3] M.B. Battles, J.P. Langedijk, P. Furmanova-Hollenstein, et al., Nat. Chem. Biol. 12 (2015) 87–93.
[4] G. Waterer, Breathe 17 (2021) 210087.
[5] H. Wang, K. Xue, P. Li, et al., Anal. Chem. 90 (2018) 6020–6027.
[6] E. Song, Y. Lai, H. Lu, et al., J. Mater. Chem. B 10 (2022) 8186–8192.
[7] Y. Ma, B. Guo, J.Y. Ge, et al., Anal. Chem. 94 (2022) 12383–12390.
[8] J. Zhang, W. Han, X. Zhou, et al., Anal. Chem. 95 (2023) 11785–11792.
[9] L. Huang, L. Zhu, W. Su, et al., Anal. Chem. 94 (2022) 11643–11649.
[10] H. Xiao, P. Li, W. Zhang, et al., Chem. Sci. 7 (2016) 1588–1593.
[11] H. Wang, M. Dong, H. Wang, et al., Chem. Commun. 57 (2021) 5838–5841.
[12] S. Wu, Y. Yan, H. Hou, et al., Anal. Chem. 94 (2022) 11238–11247.
[13] C. Liu, J. Yin, B. Lu, et al., Sens. Actuator. B: Chem. 346 (2021) 130448.
[14] J. Yin, M. Peng, W. Lin, Chem. Commun. 55 (2019) 11063–11066.
[15] J. Lung, M.S. Hung, T.Y. Wang, et al., Int. J. Mol. Sci. 23 (2022) 12533.
[16] M. Jiang, X. Gu, J.W.Y. Lam, et al., Chem. Sci. 8 (2017) 5440–5446.
[17] P. Ye, H. Zhang, J. Qu, et al., Org. Biomol. Chem. 20 (2022) 9184–9191.
[18] Y. Pu, R. Huang, L. Chai, et al., Sens. Actuator. B: Chem. 380 (2023) 133343.
[19] C. Jin, P. Yuan, Oncol. Lett. 20 (2020) 2091–2104.
[20] Q. Hu, W. Zhu, J. Du, et al., Chem. Commun. 59 (2023) 294–297.
[21] H. Jin, C. Ju, C. Duan, et al., Chem. Commun. 60 (2024) 1100–1103.
[22] Y. Sun, X. Zhou, L. Sun, et al., Chin. Chem. Lett. 33 (2022) 4229–4232.
[23] Y. Liu, L. Zhang, K. Liu, et al., Chin. Chem. Lett. 35 (2024) 109759.
[24] J. Ding, R. Xiao, A. Bi, et al., Chin. Chem. Lett. 34 (2023) 108273.
[25] B. Zhu, X. Xing, J. Kim, et al., Biomaterials 304 (2024) 122419.
[26] Y. Pang, M. Lu, H. Rha, et al., Sci. China Chem. 67 (2023) 774–787.
[27] Y. Yang, M. Ma, L. Shen, et al., Angew. Chem. Int. Ed. 62 (2023) e202310408.
[28] X. Li, X. Li, H. Ma, Chem. Sci. 11 (2019) 1617–1622.
[29] T. Zhang, F. Huo, W. Zhang, et al., Chem. Eng. J. 437 (2022) 135397.
[30] L. Long, W. Liu, P. Ruan, et al., Anal. Chem. 94 (2022) 2803–2811.
[31] Y. Tang, S. Song, J. Peng, et al., J. Mater. Chem. B 10 (2022) 6974–6982.
[32] R. Chen, Z. Li, C. Peng, et al., Anal. Chem. 94 (2022) 13432–13439.
[33] R. Wang, B. Li, S. M, et al., J. Genet. Genomics 47 (2020) 69–83.
[34] F. Amin, F. Fathi, Ž. Reiner, et al., Arch. Med. Sci. 18 (2021) 141–152.
[35] H. Chen, J. Dong, L. Yang, et al., Anal. Biochem. 668 (2023) 115114.
[36] Y. Wang, X. Han, X. Zhang, et al., Analyst 145 (2020) 1389–1395.
[37] L. Sun, M. Zou, L. Du, et al., Chem. Commun. 59 (2023) 1389–12735.
[38] G. Ma, Z. Guo, X. Zhang, et al., Sens. Actuator. B: Chem. 411 (2024) 135738.